


## Article

# Deactivation of Pd/SSZ-13 by Potassium and Water for Passive NO<sub>x</sub> Adsorption

Chi Fan <sup>1,†</sup> , Jinxing Mi <sup>2,†</sup>, Qin Wu <sup>3</sup>, Jianjun Chen <sup>1,\*</sup> and Junhua Li <sup>1</sup>

<sup>1</sup> State Key Joint Laboratory of Environment Simulation and Pollution Control, National Engineering Laboratory for Multi Flue Gas Pollution Control Technology and Equipment, School of Environment, Tsinghua University, Beijing 100084, China; fanchi@mail.tsinghua.edu.cn (C.F.); lijunhua@tsinghua.edu.cn (J.L.)

<sup>2</sup> State Key Laboratory of Catalysis, Dalian Institute of Chemical Physics, Chinese Academy of Sciences, Dalian 116023, China; mijinxing@dicp.ac.cn

<sup>3</sup> Key Laboratory of Material Chemistry for Energy Conversion and Storage, Ministry of Education, School of Chemistry and Chemical Engineering, Huazhong University of Science and Technology, Wuhan 430074, China; wuqinlx@163.com

\* Correspondence: chenjianjun@tsinghua.edu.cn

† These authors contributed equally to this work.

**Abstract:** The passive NO<sub>x</sub> adsorber (PNA) material has been considered an effective candidate for the control of NO<sub>x</sub> from diesel exhaust during the engine cold start stage, and Pd/SSZ-13 attracts peoples' attention mainly due to its superior hydrothermal stability and sulfur resistance. However, chemical poisoning tolerance of Pd/SSZ-13 is another key parameter to its practical application and future development. Herein, we prepared potassium-loaded Pd/SSZ-13 and evaluated the influence on NO<sub>x</sub> adsorption ability. The characterization results revealed that the loading of potassium could not destruct the structure of SSZ-13 but impaired the BET surface area and pore structure through the sintering of Pd species to PdO. Meanwhile, the grown PdO phase restrained the NO<sub>x</sub> adsorption ability and promoted the generation of NO<sub>2</sub> at high temperatures. Moreover, the presence of H<sub>2</sub>O could also impair the NO<sub>x</sub> adsorption ability due to the competitive adsorption between H<sub>2</sub>O and NO<sub>x</sub>. This work verifies that the design of Pd/SSZ-13 sample with stable Pd species and excellent hydrophobicity is significant for its further application under harsh conditions.

**Keywords:** passive NO<sub>x</sub> adsorption; Pd/SSZ-13; potassium poisoning; sintering of Pd species; inhibition of water



**Citation:** Fan, C.; Mi, J.; Wu, Q.; Chen, J.; Li, J. Deactivation of Pd/SSZ-13 by Potassium and Water for Passive NO<sub>x</sub> Adsorption. *Processes* **2022**, *10*, 222. <https://doi.org/10.3390/pr10020222>

Academic Editors: Chi He and Zhiming Liu

Received: 27 December 2021

Accepted: 20 January 2022

Published: 25 January 2022

**Publisher's Note:** MDPI stays neutral with regard to jurisdictional claims in published maps and institutional affiliations.



**Copyright:** © 2022 by the authors. Licensee MDPI, Basel, Switzerland. This article is an open access article distributed under the terms and conditions of the Creative Commons Attribution (CC BY) license (<https://creativecommons.org/licenses/by/4.0/>).

## 1. Introduction

The release of nitrogen oxides (NO<sub>x</sub>) from mobile sources brings huge damage to both the environment and human health; thus, diesel exhaust purification is a long-term and severe challenge in this field [1–3]. To solve the problem, urea selective catalytic reduction (Urea-SCR/NH<sub>3</sub>-SCR) technology has been successfully applied for the control of NO<sub>x</sub> release in tail gas commercially. However, unremitting efforts are still being taken to meet the increasingly rigorous requirement for the NO<sub>x</sub> emission, especially during the engine cold start period [4–7]. The exhaust temperature is almost below 200 °C during the cold start stage, which is a short time of 1~3 min upon engine starting [6–8]. However, such low temperature could not guarantee the decomposition of urea (>180 °C) and the operation of NH<sub>3</sub>-SCR process (>200 °C). Therefore, a large emission of unpurified NO<sub>x</sub> into the atmosphere is inevitable at this stage [9–11]. Particularly, stricter demands for NO<sub>x</sub> emission have been raised by Europe, USA and China in recent years [12–14], so it is extremely essential and urgent to reduce the NO<sub>x</sub> emitted in the cold start period.

Currently, many efforts have been taken to design passive NO<sub>x</sub> adsorber (PNA) materials to reduce the NO<sub>x</sub> emission through storing NO<sub>x</sub> at low temperatures (<150 °C) and releasing the adsorbed NO<sub>x</sub> at high temperatures (>200 °C), which attract significant

attention due to the promising application for NO<sub>x</sub> control in the cold start period [2,6–9]. Most PNA materials usually use noble metal (e.g., Pd and Pt) as an active adsorption center to improve the NO<sub>x</sub> storage efficiency [15–17]. Meanwhile, metal oxides, such as Al<sub>2</sub>O<sub>3</sub> and CeO<sub>2</sub>, are commonly used as carriers to possess noble metals to prepare PNA materials [6,7,18–20]. However, the existence of sulfur severely weakens the NO<sub>x</sub> adsorption ability of these metal oxide-based PNA materials, limiting their application in real exhaust condition [8,21,22]. Based on this, other materials (like zeolites) with high surface area, abundant acid sites, individual skeleton structure and superior resistance to sulfur poisoning attract much attention. Coincidentally, zeolites have been widely used as NH<sub>3</sub>-SCR catalysts worldwide, further proving its application potential as the support of applicable PNA material [5–7,23,24]. In 2016, Jonson Matthey first reported that Pd-based zeolites (Pd/CHA, Pd/MFI and Pd/BEA) exhibited high NO<sub>x</sub> storage efficiency at 100 °C and with excellent resistance to SO<sub>2</sub> at the same time [8]. Afterwards, various research with respect to the effect of zeolite structure [25], active sites [8,25], Si/Al and Pd/Al ratio [10,11], adsorption chemistry [26] and activation method [9,22] to improve NO<sub>x</sub> adsorption ability, has been carried out. Thereinto, the Pd/SSZ-13 zeolite with microporous exhibits huge application potential due to its excellent NO<sub>x</sub> storage performance and outstanding hydrothermal stability. Notably, Pd is verified to play a key role in the NO<sub>x</sub> adsorption as an active site by Szanyi et al. [15]. During the application of PNA materials for NO<sub>x</sub> adsorption, its stability is a predominant parameter for the actual use in automobile industry because of the severe working conditions with various impurities and high working temperature. Specifically, resistance ability to hydrothermal and chemical poisoning, which have been widely discussed in NH<sub>3</sub>-SCR catalysts, are also typical challenges for PNA materials [27–33]. Aiming at these problems, Kim et al. [22] found optimum hydrothermal aging treatment could enhance the NO<sub>x</sub> adsorption activity by redistributing PdO into dispersed Pd<sup>2+</sup> ions over Pd/SSZ-13. Nevertheless, sintering of PdO may occur predominantly when excessive Pd was loaded. Moreover, Khivantsev et al. [34] analyzed the hydrothermal stability of Pd/BEA zeolites with different crystal sizes and found that the larger crystals were beneficial for the well-dispersion of Pd species, and the improvement of hydrothermal aging resistance was due to the hydrophobicity of zeolite.

Although hydrothermal poisoning of Pd/SSZ-13 has been carefully studied so far, investigation about the chemical poisoning on Pd/SSZ-13 used for NO<sub>x</sub> adsorption is rarely reported. As is known, additives and impurities, derived from fuel and lubricating oil, may deposit on the catalysts and result in performance degradation due to the pore blocking and loss of active sites [27,28,31,35,36]. Both Beale et al. [35] and Li et al. [36] studied chemical deactivation on Cu/SSZ-13 caused by various impurities; it was found that the zeolite structure as well as catalytic activity were seriously affected because of the redistribution of metal species. Thereinto, K is a common element in the urea solution and biodiesel fuel used in the diesel trucks, and it can be deposited in the downstream catalyst (i.e., DOC, PNA, SCR catalyst) via the engine exhaust. Therefore, it is believed that the study of chemical deactivation of PNA material is also quite essential for the optimization of NO<sub>x</sub> adsorption ability. However, there are very few studies in the open literature concerning the chemical deactivation of K on Pd/SSZ-13, which is used for passive NO<sub>x</sub> adsorbers in diesel after-treatment system.

In this work, chemical deactivation of Pd/SSZ-13 was simulated by impregnating potassium with different contents (0.5, 1.0 and 1.5 mmol/g<sub>catal</sub>) on the fresh sample. The interaction of the zeolite framework and Pd species were characterized by various kinds of techniques. Meanwhile, the discrepancies of NO<sub>x</sub> adsorption performance between fresh and poisoned samples were analyzed. As far as we know, the effect of potassium on Pd/SSZ-13 for NO<sub>x</sub> adsorption has rarely been reported. In addition, considering the water exists in the exhaust, the potential effect of water on PNA performance was also evaluated. This work gives us a deep understanding about the degeneration of NO<sub>x</sub> adsorption ability

over Pd/SSZ-13 by chemical deactivation and water, which provides valuable information for further design of high efficiency PNA material.

## 2. Materials and Methods

### 2.1. Sample Preparation

NH<sub>4</sub>/SSZ-13 support with Si/Al ratio of 6 was prepared by a traditional hydrothermal method [37]. Fresh Pd/SSZ-13 with 1 wt.% Pd was synthesized via a “modified ion exchange method” [15] to ensure that the vast majority of Pd species are in the form of Pd<sup>2+</sup> ions. The potassium poisoned Pd/SSZ-13 was obtained by a traditional wet-impregnated method. In detail, the KNO<sub>3</sub> aqueous solution was used as a potassium source, and the amount of potassium loading was precisely controlled by adjusting the source concentration. Afterwards, the wet sample was dried at room temperature for 3 days and finally calcined at 550 °C for 3 h. The desired potassium content was 0.5, 1.0 and 1.5 mmol/g<sub>catal</sub>, and the corresponding samples were named as 0.5K-Pd/SSZ-13, 1.0K-Pd/SSZ-13 and 1.5K-Pd/SSZ-13, respectively.

### 2.2. Sample Characterization

Powder X-ray diffraction (XRD) was performed on a Rigaku SmartLab 9KW X-ray powder diffractometer with a Cu K $\alpha$  radiation. The spectra were obtained between 5 and 40°. BET surface area and pore volume were obtained by N<sub>2</sub> physisorption ASAP 2460. Before the test, the K/Pd-SSZ-13 samples were degassed at 300 °C for 3 h. The chemical state of Pd species was analyzed by Raman spectroscopy (Horiba, Japan). The content of K and Pd was measured by ICP-AES using Thermo Icap 7000. <sup>27</sup>Al MAS NMR was conducted on an Agilent 600 MHz solid state NMR spectrometer, and 0.1 M aqueous AlCl<sub>3</sub> solution was used as a reference. The dispersion of Pd species was observed by transmission electron microscopy (STEM, JEOL, JEM 2100F).

### 2.3. Evaluation of NO<sub>x</sub> Adsorption Performance

The NO<sub>x</sub> adsorption performance was evaluated in a fixed bed with powder samples (100 mg, 40–60 mesh) loaded in a quartz tube. A three-way valve was used to switch the gas between the mixing tank and reactor. Firstly, the sample was treated in 10% O<sub>2</sub>/N<sub>2</sub> (the total flow rate maintains at 200 mL/min) at 500 °C for 1 h and cooled to 100. Then approximately 220 ppm of NO<sub>x</sub> (including NO and inevitable NO<sub>2</sub>) and 5% H<sub>2</sub>O (when used) was added into the mixture gas. Once the mixed gas concentration was stable, NO<sub>x</sub> storage was performed for 1200 s at 100 °C. In the next step, the sample was heated to 500 °C at a ramping rate of 10 °C/min. The outlet gas was monitored by an online gas analyzer (MKS MultiGas 2030 FTIR). The amount of adsorption and desorption NO and NO<sub>2</sub> was calculated by the integral area, and the quantitative value was marked in the figure.

## 3. Results and Discussion

### 3.1. XRD and <sup>27</sup>Al NMR

To probe the structural changes after K impregnation, XRD patterns of fresh and deactivated samples were conducted. As shown in Figure 1, the fresh Pd/SSZ-13 exhibits typical CHA structure. No distinct Pd species are observed in all samples, probably due to the Pd phases that usually overlap with the CHA characteristic peaks [9,21]. Besides, it is observed that CHA phases of the sample impregnated with K decreased in intensity compared to the fresh sample. However, even after a high K content (1.50 mmol/g<sub>catal</sub>) is loaded, main CHA features are obviously detected and no amorphous phases are observed, indicating that the zeolite framework is still well maintained. Therefore, it could be implied that a significant disruptive impact on the zeolite framework, such as destruction or collapse, may not take place in K impregnated samples. This observation is quite different from the early report [36].

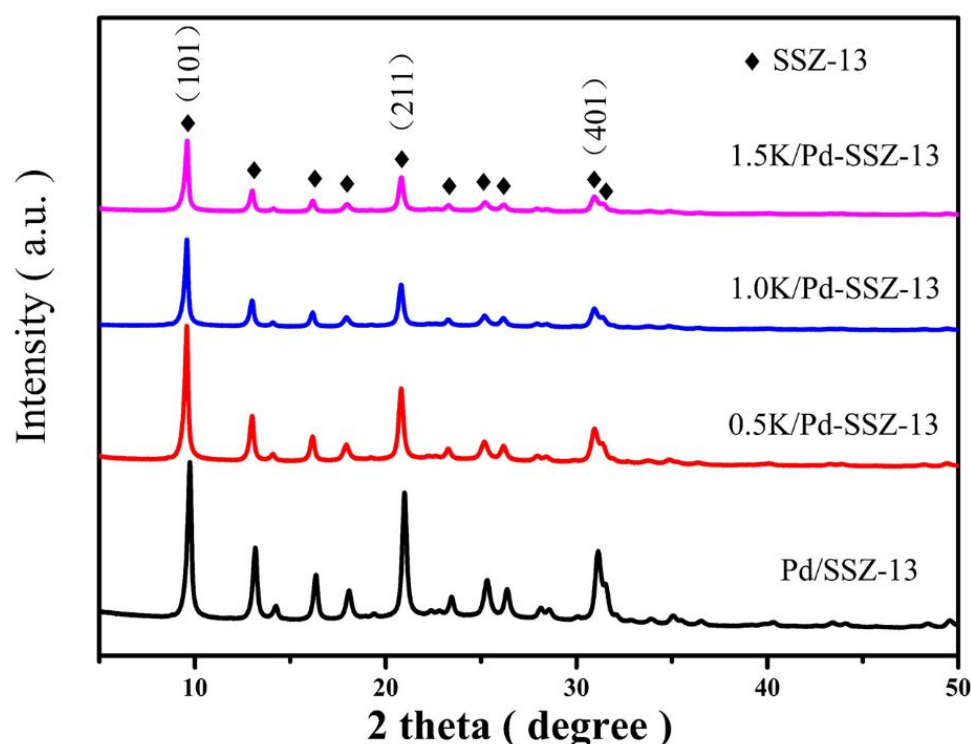


**Figure 1.** XRD patterns of Pd/SSZ-13 and K-deactivated samples.

As a more sensitive method to examine the dealumination and destruction of zeolite,  $^{27}\text{Al}$  NMR analysis is performed to evaluate framework changes in CHA structures of deactivated samples. As exhibited in Figure 2, an intense feature at 58 ppm corresponded to tetrahedral Al (framework Al), a shoulder peak of this feature caused by the distortion of  $\text{AlO}_4^-$  tetrahedra, and a broad peak centered at about 0 ppm assigned to octahedral Al (extra-framework Al) were observed [38–40]. After impregnated by K up to 1.50 mmol/g<sub>catal</sub>, the intensity of  $\text{AlO}_4^-$  tetrahedra obviously increases with increasing the K content, indicating the formation of more  $\text{AlO}_4^-$  tetrahedra. It is probably due to that the impregnation of K, which is a cation with large ionic radius, cause the change of T-O-T angle [40]. In addition, the intensity of tetrahedral Al is nearly identical to the fresh counterpart, indicating the addition of K has no significant effect on the Al framework. Such a result explicitly demonstrates that the CHA structures are relatively preserved in deactivated samples.

### 3.2. $\text{N}_2$ Physisorption and TEM

The  $\text{N}_2$  physisorption results of samples are shown in Table 1 and Table S1, and Figure S1 displays the  $\text{N}_2$  physisorption isotherms. It can be concluded that all the samples are microporous structure according to the type I isotherm. Based on the surface area and pore volume results, increasing the K content obviously decreases both the surface area and pore volume, especially the  $S_{\text{micro}}$  and  $V_{\text{micro}}$ , indicating the K loading mainly affects the micropores. This phenomenon is also supported by pore size distributions shown in Figure S2, which is evidenced by the obvious decrease in the number of pores smaller than 2 nm. Combined with the XRD and  $^{27}\text{Al}$  NMR results, it is known that the collapse of zeolite structure is not severe, thus such a decline is mainly due to the blockage of channels and pores in the zeolite framework.

To visualize the K addition on the effect of Pd species, TEM was performed for all samples, and the result is shown in Figure 3. No evident dark contrasts are observed for the Pd/SSZ-13, indicating a well dispersed Pd species in the pure Pd/SSZ-13. After K addition, some dark blocks (circled in yellow) corresponded to large Pd clusters and dark spots (circled in red) assigned to small Pd particles are clearly detected. Additionally,

by increasing the K content, the Pd clusters grow larger and become more evident. The average size of Pd clusters (calculated by the circled Pd species) is 4.9, 6.6 and 28.7 nm for 0.5K-Pd/SSZ-13, 1.0K-Pd/SSZ-13 and 1.5K-Pd/SSZ-13, respectively. It strongly suggests that the K addition promotes the sintering of Pd species. For the 1.5K-Pd/SSZ-13, some large Pd clusters are clearly observed on the crystal surface, indicating an aggregation of Pd species on the surface of zeolite after a large content of K loaded. This observation could be attributed to the fact that some Pd grains migrate and agglomerate to clusters out of the zeolite framework, or the Pd species grow larger in the zeolite pores and eventually break the zeolite structure. As proved above, the zeolite collapse of 1.5K-Pd/SSZ-13 is limited. Therefore, it is reasonable to estimate a facile migration of Pd species with potassium loading.

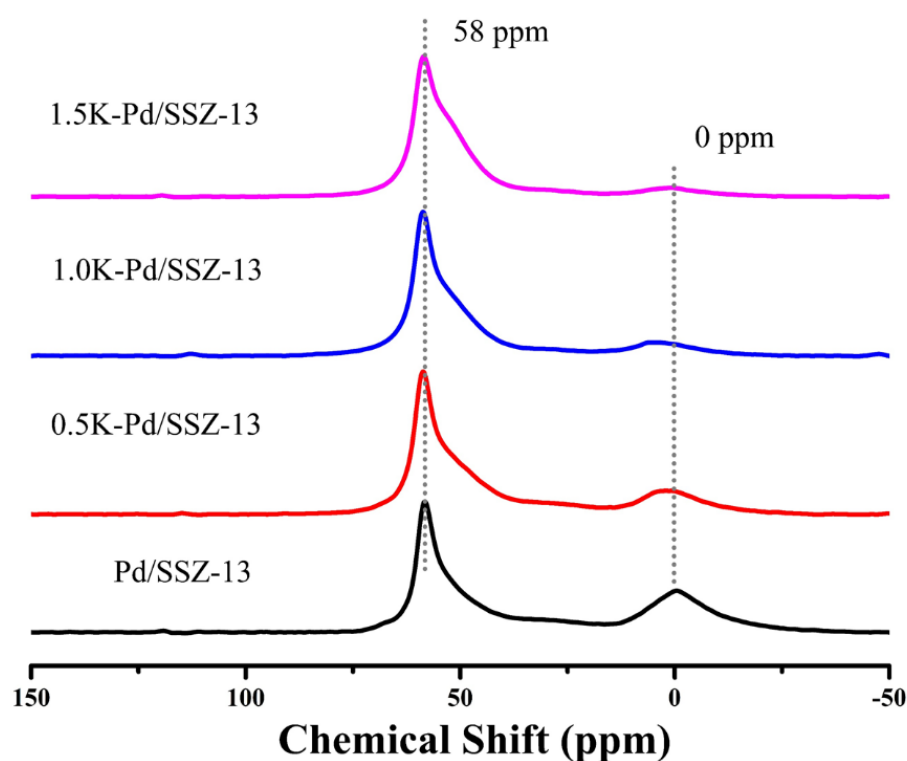


**Figure 2.**  $^{27}\text{Al}$  NMR patterns of Pd/SSZ-13 and K-deactivated samples.

**Table 1.** Physicochemical property of Pd/SSZ-13 and K-deactivated samples.

Sample	$S_{\text{BET}}$ m <sup>2</sup> /g	Pore Volume cm <sup>3</sup> /g	Pd Content wt. %	K Content wt. %
Pd/SSZ-13	392	0.23	0.96	-
0.5K-Pd/SSZ-13	348	0.21	0.94	1.81
1.0K-Pd/SSZ-13	318	0.19	0.92	3.52
1.5K-Pd/SSZ-13	262	0.15	0.90	5.41

### 3.3. Raman

As evidenced by N<sub>2</sub> physisorption and TEM results, the sintering of Pd species is responsible for the blockage of zeolite pores and channels. Raman analysis was performed to confirm the sintering species. As shown in Figure 4, a Raman shift at around 650 cm<sup>−1</sup> assigned to bulk PdO is clearly observed for potassium-deactivated samples [41]. The peak intensity becomes even larger with increasing potassium content, which demonstrates that the bulk PdO is the dominant sintering species. With regard to the formation of PdO, it is reasonable to speculate that the addition of K facilitates the Pd<sup>2+</sup> to migrate out of ion-exchange sites and eventually aggregate to the PdO during the following calcination



process. In this manner, the migration of  $\text{Pd}^{2+}$  is accelerated and more  $\text{Pd}^{2+}$  is sintering after excess K loaded and thus clustered  $\text{PdO}$  is much more observable.

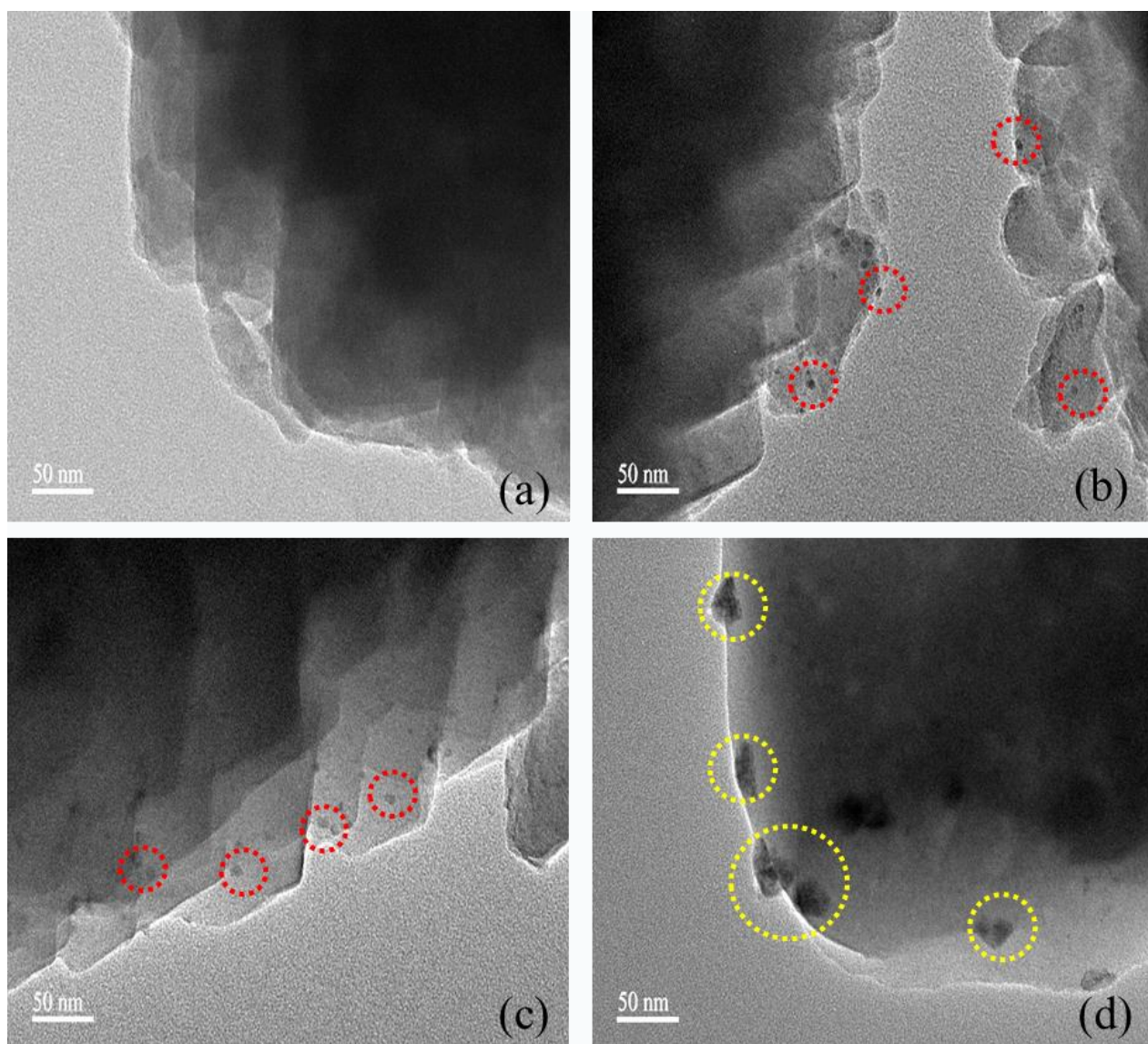


**Figure 3.** TEM images of the (a) Pd/SSZ-13 and K-deactivated samples (b) 0.5K-Pd/SSZ-13, (c) 1.0K-Pd/SSZ-13 and (d) 1.5K-Pd/SSZ-13. The red and yellow circle represents aggregated Pd clusters.

### 3.4. PNA Performance

Compared to the influences of K on Cu/SSZ-13 and Cu-SAPO-34, the deleterious effects on Pd/SSZ-13 are much more significant. For example, after loading 1.0 and 1.5 mmol/g<sub>catal</sub>, the decrease in  $S_{\text{BET}}$  and SCR performance of Cu/SSZ-13 was quite small [37], in the contrary, the blockage of channels and pores in Pd/SSZ-13 was much more serious and an obvious deterioration in  $\text{NO}_x$  adsorption was observed. In addition, the influence of K on the original active metal sites in zeolite is quite different. After introducing K, the aggregation of Cu species in Cu/SSZ-13 was not easily detected. However, large Pd clusters were displayed in all K-deactivated catalysts shown in SEM images. Thus, it is suggested that the substitution of K to Pd in Pd/SSZ-13 is more likely to happen. In order to evaluate the poisoning effect of K on Pd/SSZ-13, the PNA performance of K-deactivated samples was tested. As shown in Figure 5a, the results of  $\text{NO}_x$  storage at 100 °C followed by a desorption with increasing the temperature at a rate of 10 °C/min to 500 °C is depicted, and the profiles of NO and  $\text{NO}_2$  are recorded separately to obtain an unambiguous

understanding of respective trapping and desorption behaviors. The NO and NO<sub>2</sub> inlet concentrations are about 210 and 10 ppm, and the inevitably NO<sub>2</sub> in the feed gas probably originates from the oxidation of NO source [34]. The adsorption and desorption content were estimated by the integration of peak area and were marked in the corresponding peak. For the fresh Pd/SSZ-13, it is evident that abundant NO is trapped during the first 1200 s at 100 °C. In contrast, the NO<sub>2</sub> adsorption is few, corresponding to the one-twelfth of NO adsorbing capacity. When increasing the temperature, the trapped NO and NO<sub>2</sub> desorb simultaneously at 200 °C, and the respective desorption amount is 8.9 and 9.2 μmol. It is very impressive for forming quite a large amount of NO<sub>2</sub> since little NO<sub>2</sub> is adsorbed at the trapping step. The desorption of NO<sub>2</sub> is probably due to the decomposition of nitrate species formed by NO. After NO completely desorbs at 280 °C, the NO concentration is below 210 ppm in the temperature range of 280–550 °C, indicating NO is trapped again by Pd/SSZ-13 or consumed in the testing atmosphere. Meanwhile, a second NO<sub>2</sub> shoulder peak centering at 320 °C appears following the initial NO<sub>2</sub> desorption peak, which strongly indicates a new approach or intermediate for NO<sub>2</sub> formation different from the former. In addition, it is noted that the outlet NO and NO<sub>2</sub> concentration nearly restores to the initial level at 500 °C eventually. Therefore, it could be mentioned that the oxidation of NO to NO<sub>2</sub> by oxygen at high temperatures is limited for the Pd/SSZ-13 in our study. According to the calculated NO<sub>x</sub> concentration shown in Figure 5, it is revealed that although Pd/SSZ-13 adsorbs plenty of NO at 100 °C, the NO<sub>x</sub> desorption mainly consists of NO<sub>2</sub>. In order to illustrate the possible pathway for NO<sub>x</sub> transformation during the desorption step, oxygen is not purged to the feed gas in the heating-up period to avoid possible oxidation reactions from NO to NO<sub>2</sub>. As shown in Figure S6, the NO<sub>x</sub> adsorption ability is almost unchanged, and well-resolved NO and NO<sub>2</sub> desorption peaks are similar to Figure 5a centering at about 200 °C are also observed. Additionally, the estimated desorption amount is close to that calculated in the presence of oxygen. This result clearly reveals that the desorbed NO<sub>2</sub> at low temperatures originates from the decomposition of some chemical intermediates formed in the storage step rather than directly from the oxidation of NO in the desorption process, because oxygen is not essential for the formation of this kind of NO<sub>2</sub>. However, for the case heating up in the absence of oxygen, a new broad NO releasing profile rather than an NO storage peak shown in Figure 5a is observed between 250 and 500 °C. Meanwhile, the NO<sub>2</sub> concentration drops to zero. This observation indicates that the second NO<sub>2</sub> formation on Pd/SSZ-13 at high temperatures in the presence of oxygen simply originates from the oxidation of chemisorbed NO in Pd/SSZ-13 rather than the gas phase NO. Besides, based on the fact that two NO desorption peaks are observed in the absence of oxygen, it is reasonable to speculate that there are various adsorption sites for NO on Pd/SSZ-13. To further study the effect of oxygen on NO<sub>x</sub> adsorption, the overall test process is conducted without oxygen supplement. As observed in Figure S7, Pd/SSZ-13 mainly adsorbs NO at first 1200 s, while the adsorption ability (9.6 μmol) is much inferior to those performed in the presence of oxygen (19.8 μmol). It indicates that oxygen is beneficial for NO adsorption. A special phenomenon is that a NO<sub>2</sub> formation peak appears at the trapping step. Note that each sample is activated by oxygen before the test, thus it is possible that some NO is oxidized by the adsorbed oxygen to NO<sub>2</sub> in zeolite. When it comes to the desorption stage, two NO desorption peaks are still stable, but the released amount in the low temperature decreases a lot compared with a counterpart in Figure 5a. In addition, no NO<sub>2</sub> formation peak is observed during ramping. According to the above results, it can be concluded that: (1) oxygen enhances the NO storage capacity mainly by reacting with NO on Pd/SSZ-13 to form intermediates, which could decompose to NO<sub>2</sub> during the heating-up period; (2) The NO desorbed from Pd/SSZ-13 at higher temperature could be easily oxidized by oxygen to form NO<sub>2</sub>, which correlates to the NO<sub>2</sub> formation ranging from 280 to 500 °C; (3) The catalytic reaction of NO to NO<sub>2</sub> by oxygen is inconspicuous in our study, which is due to little PdO exists in the as-synthesized Pd/SSZ-13. The K-loaded sample exhibits poor NO storage capacity during the first 1200 s at 100 °C, especially the increased K content could severely reduce the NO adsorption performance (from 6.6 μmol of 0.5K-Pd/SSZ-13

to 3.6  $\mu\text{mol}$  of 1.5K-Pd/SSZ-13). However, the  $\text{NO}_2$  adsorption ability was not mainly affected by the addition of K. With increasing the temperature, the trapped NO and  $\text{NO}_2$  also desorb simultaneously at about 200  $^{\circ}\text{C}$ , and the respective NO desorption amounts are 2.5–1.4  $\mu\text{mol}$  and  $\text{NO}_2$  desorption amounts are 3.6–2.4  $\mu\text{mol}$  for K-Pd/SSZ-13 sample. After NO completely desorbs above 270  $^{\circ}\text{C}$ , a little negative NO peaks below 210 ppm are observed over these K-Pd/SSZ-13 samples along with an increase in  $\text{NO}_2$  content, which indicates the NO could be converted to  $\text{NO}_2$  over K-Pd/SSZ-13 samples at high temperatures. This is due to the enhanced oxidation of NO to  $\text{NO}_2$  by formed PdO.

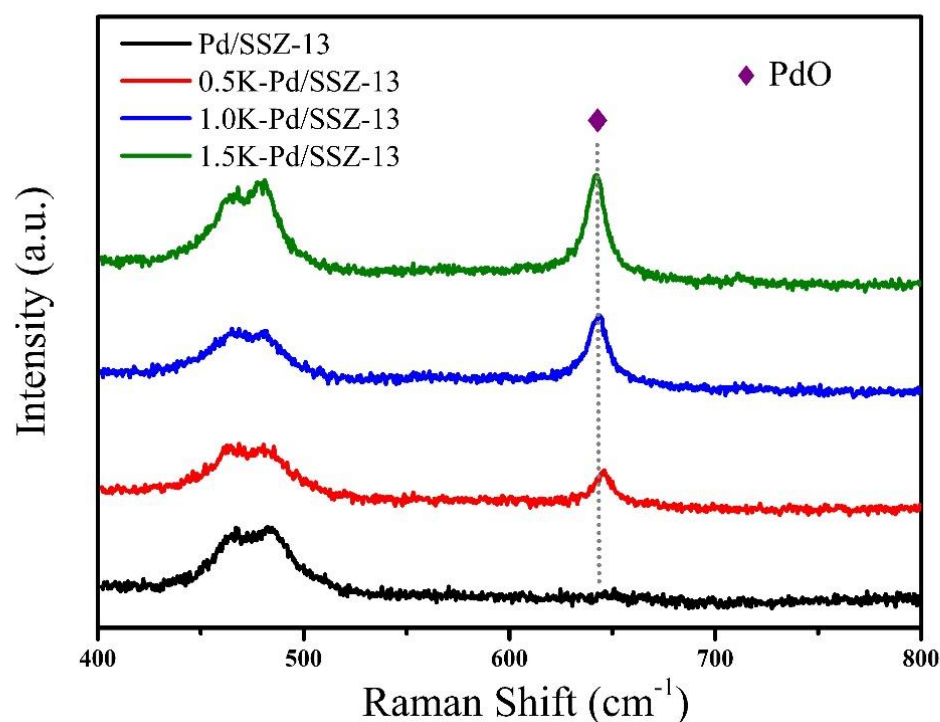
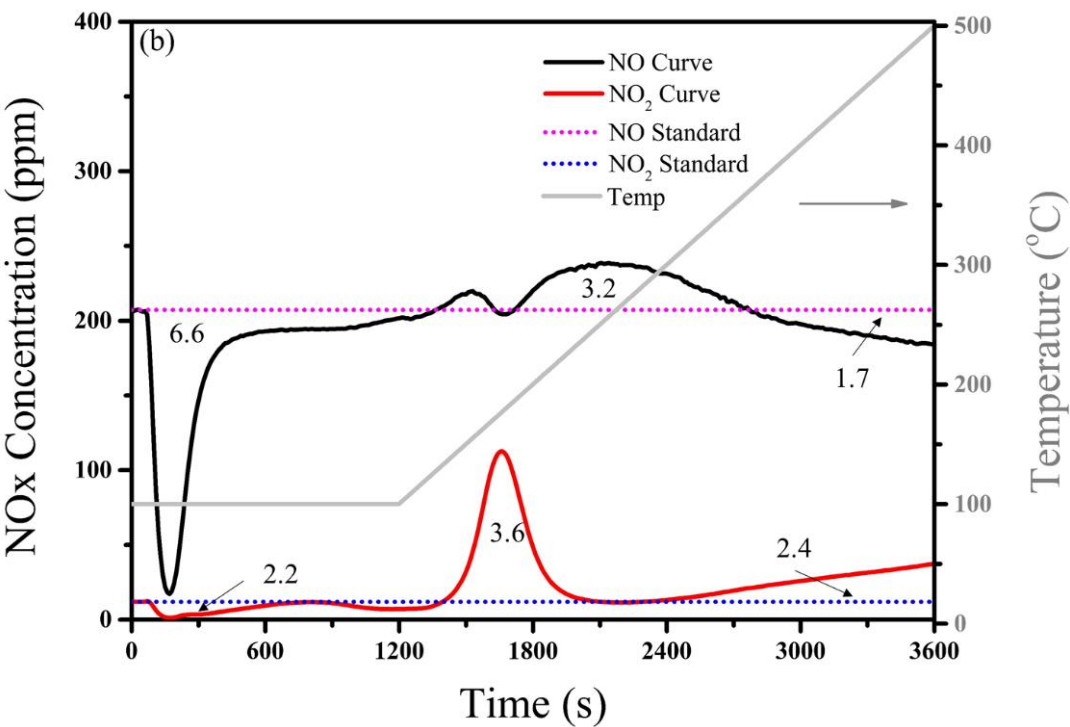
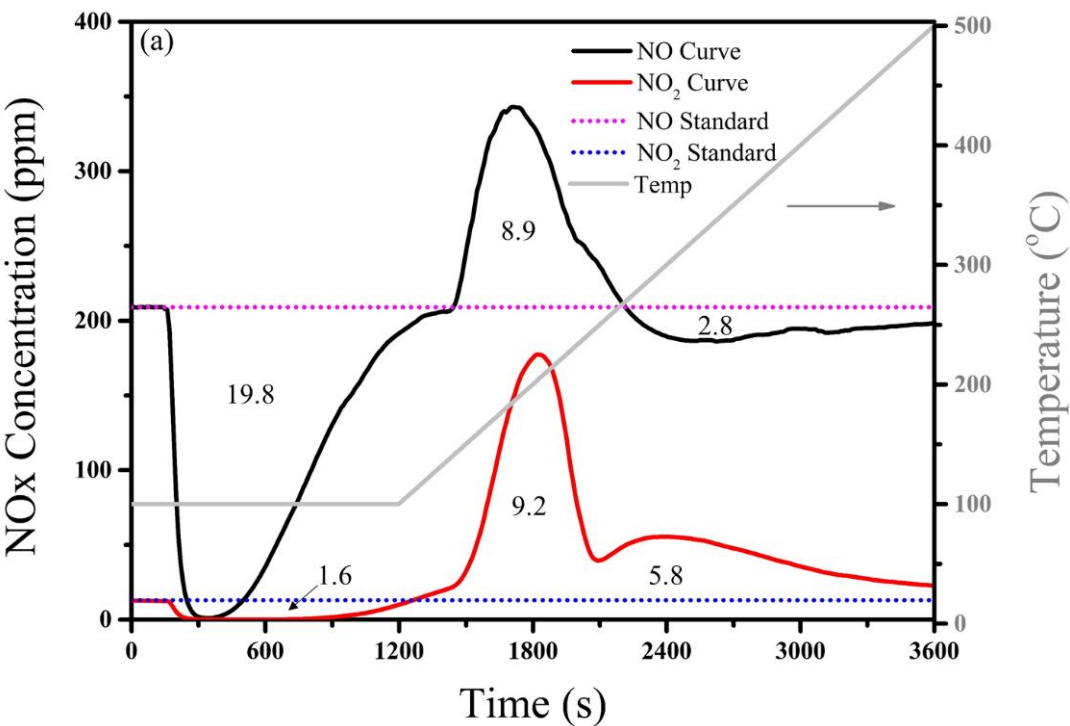


**Figure 4.** Raman spectra of the Pd/SSZ-13 and K-deactivated samples.

To better simulate the actual after-treatment condition, 5%  $\text{H}_2\text{O}$  was added to the feed gas to evaluate the water tolerance of as-prepared Pd/SSZ-13, and the PNA performance is displayed in Figure 6. Compared to the adsorption ability of fresh Pd/SSZ-13, the addition of  $\text{H}_2\text{O}$  significantly suppresses the NO adsorption on Pd/SSZ-13, as evidenced from the rapid NO saturation adsorption and much smaller total adsorption capacity. In contrast, the  $\text{NO}_2$  adsorption is found to be less affected by  $\text{H}_2\text{O}$ . In the ramping process, a second NO adsorption peak centered at 200  $^{\circ}\text{C}$  is clearly displayed. Combined with the fact that  $\text{H}_2\text{O}$  completely desorbs at around 180  $^{\circ}\text{C}$  shown in Figure S8, it is convictive to state that  $\text{H}_2\text{O}$  competes with NO to adsorb on active Pd sites at 100  $^{\circ}\text{C}$  and thus adversely affects the NO storage capacity. Immediately upon the  $\text{H}_2\text{O}$  desorption from adsorption sites that occurs at a higher temperature, the NO could be trapped again. Even though the total NO adsorption amount is still not comparable to those tested in the absence of  $\text{H}_2\text{O}$  based on the calculated amount shown in Figure 5a, probably due to the temperature above 180  $^{\circ}\text{C}$  is too high for the full adsorption of NO. With further increasing the temperature to 250  $^{\circ}\text{C}$ , an evident NO release is found, which is quite opposite for the observation in Figure 5a, indicating the oxidation of NO to  $\text{NO}_2$  is completely suppressed in the presence of  $\text{H}_2\text{O}$ . When it comes to the  $\text{NO}_2$  desorption, only a small peak appears at 190  $^{\circ}\text{C}$ . Considering most Pd active sites are occupied by  $\text{H}_2\text{O}$  during the storage step, it is reasonable to estimate that the desorbed  $\text{NO}_2$  mainly comes from physical adsorption sites such as pores and channels or the reaction between NO and the zeolite substrate. As proved by the PNA performance of H-SSZ-13 shown in Figure S9, an evident  $\text{NO}_2$  desorption peak centering at 170  $^{\circ}\text{C}$  is depicted and the amount of formed  $\text{NO}_2$  (3.4  $\mu\text{mol}$ ) is larger than that of the



adsorbed (0.6  $\mu\text{mol}$ ), proving the pure zeolite without Pd addition could still interact with NO and release respectable  $\text{NO}_2$ .



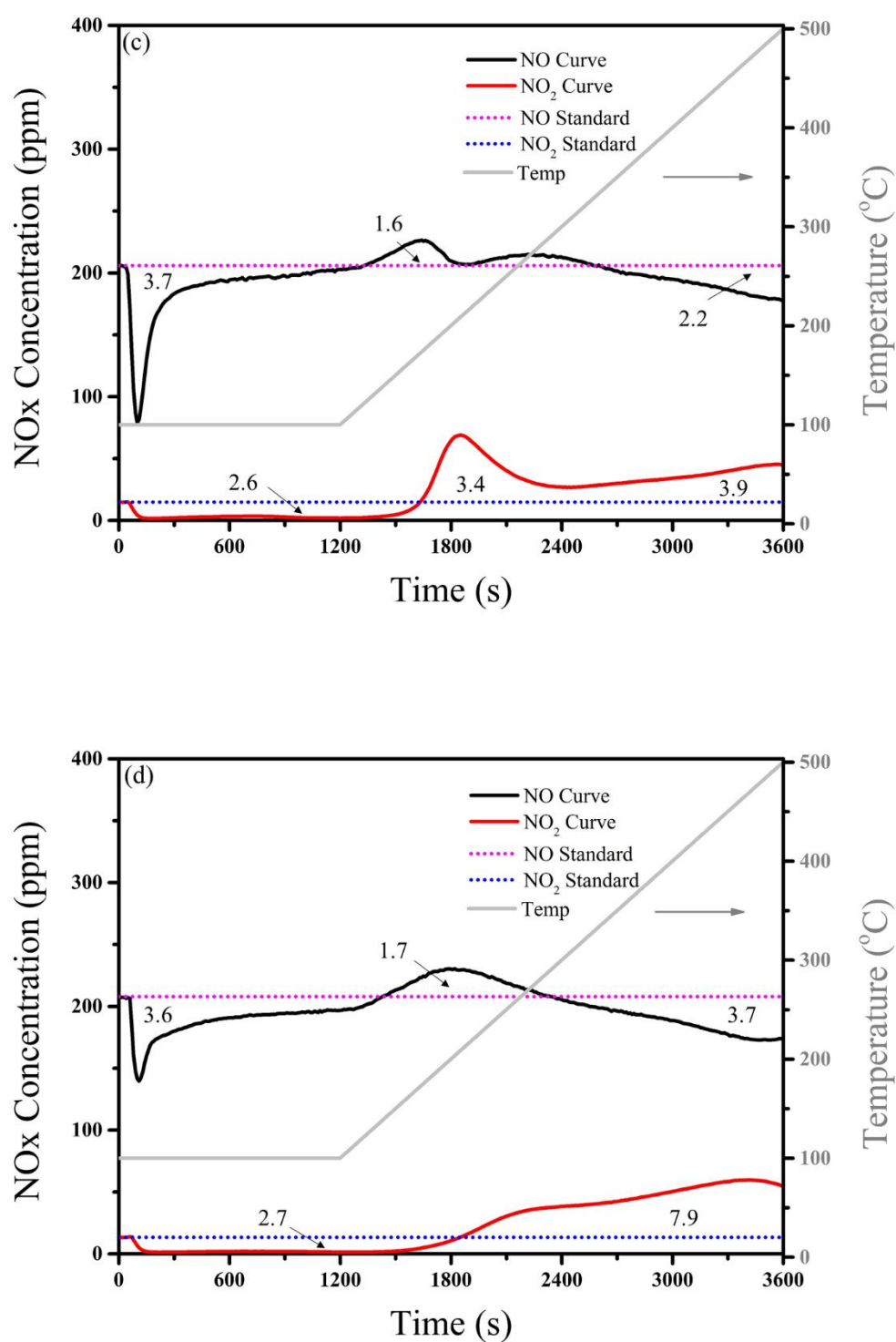


**Figure 5.** Transient NO<sub>x</sub> adsorption at 100 °C and temperature programmed desorption of (a) Pd/SSZ-13 and K-deactivated samples (b) 0.5K-Pd/SSZ-13, (c) 1.0K-Pd/SSZ-13 and (d) 1.5K-Pd/SSZ-13.

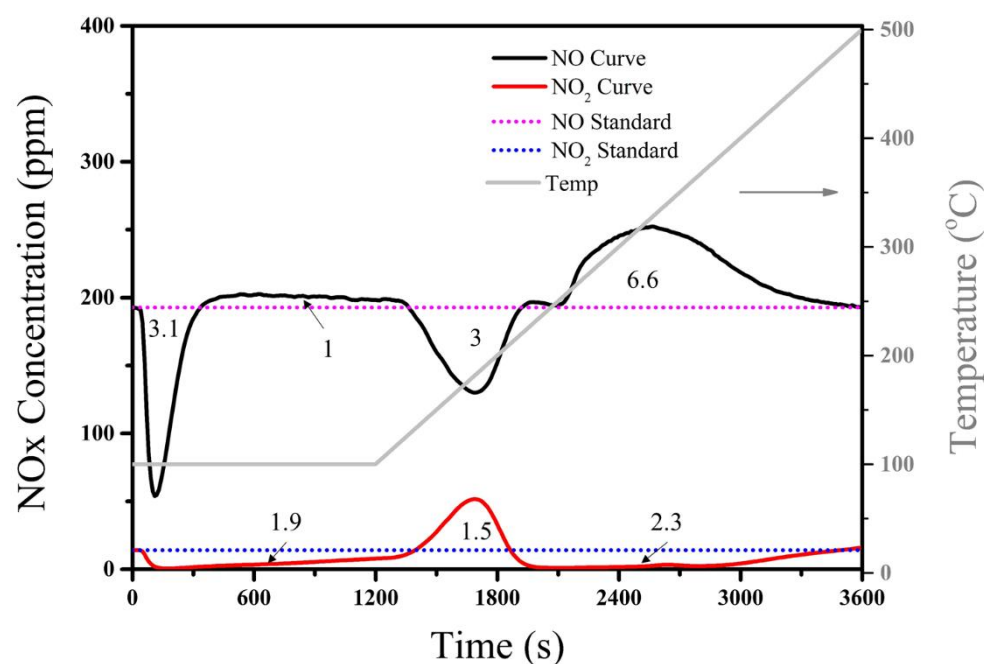


**Figure 6.** Transient NO<sub>x</sub> adsorption at 100 °C and temperature programmed desorption of as-prepared Pd/SSZ-13 when 5% H<sub>2</sub>O is added to the flow gas.

#### 4. Conclusions

In this work, the deactivation effect of potassium and water on Pd/SSZ-13 was studied. A series of potassium loaded Pd/SSZ-13 samples were prepared for the NO<sub>x</sub> adsorption ability. The Raman result demonstrated that the loading of potassium could result in the sintering of Pd species, while the XRD, NMR and BET results indicated the structure of SSZ-13 was stable and the texture parameter of Pd/SSZ-13 sample is reduced after potassium loading. Among the prepared K-Pd/SSZ-13 samples, those with free potassium are the best in NO<sub>x</sub> storage with poor water tolerance. Overall, the weakened NO<sub>x</sub> storage performance over K-deactivated Pd/SSZ-13 could be attributed to the transformation of Pd<sup>2+</sup> to PdO cluster, which was promoted by the increase in potassium content. Besides, the H<sub>2</sub>O was also found to have a negative effect on Pd/SSZ-13 due to the competitive adsorption with NO<sub>x</sub>. As a result, the hydrophobicity is significant for the zeolite-based PNA material. The research outcomes give us new insights into the poisoning mechanism of potassium and H<sub>2</sub>O for NO<sub>x</sub> adsorption and could guide the design of efficient PNA materials to control NO<sub>x</sub> emission during cold start stage.

**Supplementary Materials:** The following supporting information can be downloaded at: <https://www.mdpi.com/article/10.3390/pr10020222/s1>, Figure S1: N<sub>2</sub> physisorption isotherms of Pd/SSZ-13 and K deactivated samples; Figure S2: Pore distributions of Pd/SSZ-13 and K deactivated samples; Figure S3: Standard deviation values of 0.5K-Pd/SSZ-13; Figure S4: Standard deviation values of 1.0K-Pd/SSZ-13; Figure S5: Standard deviation values of 1.5K-Pd/SSZ-13; Figure S6: Transient NO<sub>x</sub> adsorption at 100 °C and temperature programmed desorption of Pd/SSZ-13 without O<sub>2</sub> in the heating up period; Figure S7: Transient NO<sub>x</sub> adsorption at 100 °C and temperature programmed desorption of Pd/SSZ-13 without O<sub>2</sub> in the whole test; Figure S8: Transient H<sub>2</sub>O adsorption at 100 °C and temperature programmed desorption of the Pd/SSZ-13 catalysts; Figure S9: Transient NO<sub>x</sub> adsorption at 100 °C and temperature programmed desorption of the H-SSZ-13 catalysts; Table S1: The surface area and pore volume of the samples.

**Author Contributions:** C.F. and J.M. designed the experiment, characterized samples, and wrote the manuscript. Q.W. helped to synthesize samples and test the PNA performance. J.C. and J.L. offered suggestions and revised the manuscript. All authors have read and agreed to the published version of the manuscript.

**Funding:** This research was funded by National Key R&D Program of China (2018YFC0213400), and the National Natural Science Foundation of China (21876093 and 52070114).

**Acknowledgments:** We thank the National Key R&D Program of China (2018YFC0213400), and the National Natural Science Foundation of China (21876093 and 52070114) for financial support.

**Conflicts of Interest:** The authors declare no competing financial interest.

## References

1. Shan, Y.L.; Du, J.P.; Zhang, Y.; Shan, W.P.; Shi, X.Y.; Yu, Y.B.; Zhang, R.D.; Meng, X.J.; Xiao, F.S.; He, H. Selective catalytic reduction of NO<sub>x</sub> with NH<sub>3</sub>: Opportunities and challenges of Cu-based small-pore zeolites. *Natl. Sci. Rev.* **2021**, *8*, 1–20. [\[CrossRef\]](#) [\[PubMed\]](#)
2. Walker, A. Future challenges and incoming solutions in emission control for heavy duty diesel vehicles. *Top. Catal.* **2016**, *59*, 695–707. [\[CrossRef\]](#)
3. Nova, I.; Tronconi, E. *Urea-SCR Technology for deNO<sub>x</sub> after Treatment of Diesel Exhausts*; Springer: New York, NY, USA, 2015; Volume 59, pp. 221–232.
4. Xu, L.; Lupescu, J.; Ura, J.; Harwell, A.; Paxton, W.; Nunan, J.; Alltizer, C. Benefits of Pd doped zeolites for cold start HC/NO<sub>x</sub> emission reductions for gasoline and E85 fueled vehicles. *SAE Int. J. Fuels Lubr.* **2018**, *11*, 301–307. [\[CrossRef\]](#)
5. Chen, H.Y.; Mulla, S.; Weigert, E.; Camm, K.; Ballinger, T.; Cox, J.; Blakeman, P. Cold start concept (CSC<sup>TM</sup>): A novel catalyst for cold start emission control. *SAE Int. J. Fuels Lubr.* **2013**, *6*, 372–381. [\[CrossRef\]](#)
6. Gu, Y.; Epling, W.S. Passive NO<sub>x</sub> adsorber: An overview of catalyst performance and reaction chemistry. *Appl. Catal. A Gen.* **2019**, *570*, 1–14. [\[CrossRef\]](#)
7. Lee, J.; Theis, J.R.; Kyriakidou, E.A. Vehicle emissions trapping materials: Successes, challenges, and the path forward. *Appl. Catal. B Environ.* **2019**, *243*, 397–414. [\[CrossRef\]](#)
8. Chen, H.Y.; Collier, J.E.; Liu, D.; Mantarosie, L. Low temperature NO storage of zeolite supported Pd for low temperature diesel engine emission control. *Catal. Lett.* **2016**, *146*, 1706–1711. [\[CrossRef\]](#)
9. Ryou, Y.S.; Lee, J.; Lee, H.; Kim, C.H.; Kim, D.H. Effect of various activation conditions on the low temperature NO adsorption performance of Pd/SSZ-13 passive NO<sub>x</sub> adsorber. *Catal. Today* **2017**, *320*, 175–180. [\[CrossRef\]](#)
10. Mihai, O.; Trandafilovic, L.; Wentworth, T.; Torres, F.F.; Olsson, L. The effect of Si/Al ratio for Pd/BEA and Pd/SSZ-13 used as passive NO<sub>x</sub> adsorbers. *Top. Catal.* **2018**, *61*, 2007–2020. [\[CrossRef\]](#)
11. Lee, J.; Ryou, Y.S.; Cho, S.J.; Lee, H.; Kim, C.H.; Kim, D.H. Investigation of the active sites and optimum Pd/Al of Pd/ZSM-5 passive NO adsorbers for the cold-start application: Evidence of isolated-Pd species obtained after a high-temperature thermal treatment. *Appl. Catal. B Environ.* **2018**, *226*, 71–82. [\[CrossRef\]](#)
12. Liu, Y.; Balaji, S.; Mojghan, N.; Penelope, M.; Sougato, C. After-treatment systems to meet China NS VI, India BS VI regulation limits. In Proceedings of the SAE 2017 World Congress & Exhibition—Society of Automotive Engineers, Detroit, MI, USA, 4–6 April 2017.
13. Johnson, T.; Joshi, A. Review of vehicle engine efficiency and emissions. *SAE Int. J. Adv. Curr. Prac. Mobil.* **2019**, *1*, 734–761.
14. Sharp, C.; Webb, C.C.; Yoon, S.; Henry, C.; Zavala, B. Achieving ultra low NO<sub>x</sub> emissions levels with a 2017 heavy-duty on-highway TC diesel engine-comparison of advanced technology approaches. *SAE Int. J. Engines* **2017**, *10*, 1722–1735. [\[CrossRef\]](#)
15. Khivantsev, K.; Jaegers, N.R.; Kovarik, L.; Hanson, J.C.; Tao, F.; Tang, Y.; Zhang, X.; Koleva, I.Z. Achieving atomic dispersion of highly loaded transition metals in small-pore zeolite SSZ-13: High-capacity and high-efficiency low-temperature CO and passive NO<sub>x</sub> adsorbers. *Angew. Chem. Int. E* **2018**, *57*, 16672–16677. [\[CrossRef\]](#) [\[PubMed\]](#)
16. Selleri, T.; Gramigni, F.; Nova, I. A PGM-free NO<sub>x</sub> adsorber + selective catalytic reduction catalyst system (AdSCR) for trapping and reducing NO<sub>x</sub> in lean exhaust streams at low temperature. *Catal. Sci. Technol.* **2018**, *8*, 2467–2476. [\[CrossRef\]](#)
17. Ji, Y.; Bai, S.; Crocker, M. Al<sub>2</sub>O<sub>3</sub>-based passive NO<sub>x</sub> adsorbers for low temperature applications. *Appl. Catal. B Environ.* **2015**, *170–171*, 283–292. [\[CrossRef\]](#)
18. Ji, Y.; Xu, D.; Bai, S. Pt- and Pd-Promoted CeO<sub>2</sub>-ZrO<sub>2</sub> for passive NO<sub>x</sub> adsorber applications. *Ind. Eng. Chem. Res.* **2016**, *56*, 111–125. [\[CrossRef\]](#)
19. Jones, S.; Ji, Y.; Bueno-Lopez, A. CeO<sub>2</sub>-M<sub>2</sub>O<sub>3</sub> passive NO<sub>x</sub> adsorbers for cold start applications. *Emi. Cont. Sci. Technol.* **2017**, *3*, 59–72. [\[CrossRef\]](#)
20. Jones, S.; Ji, Y.; Crocker, M. Ceria-based catalysts for low temperature NO<sub>x</sub> storage and release. *Catal. Lett.* **2016**, *146*, 909–917. [\[CrossRef\]](#)
21. Ryou, Y.; Lee, J.; Kim, Y. Effect of reduction treatments (H<sub>2</sub> vs. CO) on the NO adsorption ability and the physicochemical properties of Pd/SSZ-13 passive NO<sub>x</sub> adsorber for cold start application. *Appl. Catal. A Gen.* **2019**, *569*, 28–34. [\[CrossRef\]](#)
22. Ryou, Y.; Lee, J.; Cho, S.J. Activation of Pd/SSZ-13 catalyst by hydrothermal aging treatment in passive NO adsorption performance at low temperature for cold start application. *Appl. Catal. B Environ.* **2017**, *212*, 140–149. [\[CrossRef\]](#)
23. Beale, A.M.; Gao, F.; Lezcano-Gonzalez, I.; Peden, C.H.F.; Szanyi, J. Recent advances in automotive catalysis for NO<sub>x</sub> emission control by small-pore microporous materials. *Chem. Soc. Rev.* **2015**, *44*, 7371–7405. [\[CrossRef\]](#) [\[PubMed\]](#)
24. Wang, J.; Zhao, H.; Haller, G. Recent advances in the selective catalytic reduction of NO<sub>x</sub> with NH<sub>3</sub> on Cu-Chabazite catalysts. *Appl. Catal. B Environ.* **2017**, *202*, 346–354. [\[CrossRef\]](#)



25. Khivantsev, K.; Gao, F.; Kovarik, L. Molecular level understanding of how oxygen and carbon monoxide improve NO<sub>x</sub> storage in palladium/SSZ-13 passive NO<sub>x</sub> adsorbers: The role of NO<sup>+</sup> and Pd(II)(CO)(NO) species. *J. Phys. Chem. C* **2018**, *122*, 10820–10827. [\[CrossRef\]](#)
26. Zheng, Y.; Kovarik, L.; Engelhard, M.H. Low-temperature Pd/Zeolite passive NO<sub>x</sub> adsorbers: Structure, performance, and adsorption chemistry. *J. Phys. Chem. C* **2017**, *121*, 15793–15803. [\[CrossRef\]](#)
27. Shwan, S.; Jansson, J.; Olsson, L. Chemical deactivation of H-BEA and Fe-BEA as NH<sub>3</sub>-SCR catalysts-effect of potassium. *Appl. Catal. B Environ.* **2015**, *166–167*, 277–286. [\[CrossRef\]](#)
28. Chen, Z.; Fan, C.; Pang, L. The influence of phosphorus on the catalytic properties, durability, sulfur resistance and kinetics of Cu-SSZ-13 for NO<sub>x</sub> reduction by NH<sub>3</sub>-SCR. *Appl. Catal. B Environ.* **2018**, *237*, 116–127. [\[CrossRef\]](#)
29. Kim, Y.J.; Lee, J.K.; Min, K.M. Hydrothermal stability of CuSSZ13 for reducing NO<sub>x</sub> by NH<sub>3</sub>. *J. Catal.* **2014**, *311*, 447–457. [\[CrossRef\]](#)
30. Kwak, J.H.; Tran, D.; Burton, S.D. Effects of hydrothermal aging on NH<sub>3</sub>-SCR reaction over Cu/zeolites. *J. Catal.* **2012**, *287*, 203–209. [\[CrossRef\]](#)
31. Ma, J.; Si, Z.; Weng, D. Potassium poisoning on Cu-SAPO-34 catalyst for selective catalytic reduction of NO<sub>x</sub> with ammonia. *Chem. Eng. J.* **2015**, *267*, 191–200. [\[CrossRef\]](#)
32. Zhang, T.; Qiu, F.; Li, J. Design and synthesis of core-shell structured meso-Cu-SSZ-13@mesoporous aluminosilicate catalyst for SCR of NO with NH<sub>3</sub>: Enhancement of activity, hydrothermal stability and propene poisoning resistance. *Appl. Catal. B Environ.* **2016**, *195*, 48–58. [\[CrossRef\]](#)
33. Ma, L.; Cheng, Y.; Cavataio, G. Characterization of commercial Cu-SSZ-13 and Cu-SAPO-34 catalysts with hydrothermal treatment for NH<sub>3</sub>-SCR of NO<sub>x</sub> in diesel exhaust. *Chem. Eng. J.* **2013**, *225*, 323–330. [\[CrossRef\]](#)
34. Khivantsev, K.; Jaegers, N.R.; Kovarik, L. Palladium/Beta zeolite passive NO<sub>x</sub> adsorbers (PNA): Clarification of PNA chemistry and the effects of CO and zeolite crystallite size on PNA performance. *Appl. Catal. A Gen.* **2019**, *569*, 141–148. [\[CrossRef\]](#)
35. Lezcano-Gonzalez, I.; Deka, U. Chemical deactivation of Cu-SSZ-13 ammonia selective catalytic reduction (NH<sub>3</sub>-SCR) systems. *Appl. Catal. B Environ.* **2014**, *154–155*, 339–349. [\[CrossRef\]](#)
36. Fan, C.; Chen, Z.; Pang, L. Steam and alkali resistant Cu-SSZ-13 catalyst for the selective catalytic reduction of NO<sub>x</sub> in diesel exhaust. *Chem. Eng. J.* **2018**, *334*, 344–354.
37. Song, J.; Wang, Y.; Walter, E.D. Toward rational design of Cu/SSZ-13 selective catalytic reduction catalysts: Implications from atomic-level understanding of hydrothermal stability. *ACS Catal.* **2017**, *7*, 8214–8227. [\[CrossRef\]](#)
38. Han, S.; Cheng, J.; Zheng, C.; Ye, Q.; Cheng, S.; Kang, T.; Dai, H.X. Effect of Si/Al ratio on catalytic performance of hydrothermally aged Cu-SSZ-13 for the NH<sub>3</sub>-SCR of NO in simulated diesel exhaust. *Appl. Surf. Sci.* **2017**, *419*, 382–392. [\[CrossRef\]](#)
39. Gao, F.; Charles, P. Effects of alkali and alkaline earth cocations on the activity and hydrothermal stability of Cu-SSZ-13 NH<sub>3</sub>-SCR Catalysts. *ACS Catal.* **2015**, *5*, 6780–6791. [\[CrossRef\]](#)
40. Lv, W.; Li, J.; Fan, W. Regulation of Al distributions and Cu<sup>2+</sup> locations in SSZ-13 zeolites for NH<sub>3</sub>-SCR of NO by different alkali metal cations. *J. Catal.* **2021**, *393*, 190–201. [\[CrossRef\]](#)
41. Lee, J.; Ryou, Y.S.; Hwang, S.; Kim, Y.; Cho, S.J.; Lee, H.; Kim, C.H.; Kim, D.H. Comparative study of the mobility of Pd species in SSZ-13 and ZSM-5, and its implication for their activity as passive NO<sub>x</sub> adsorbers (PNAs) after hydrothermal aging. *Catal. Sci. Technol.* **2019**, *9*, 163–173. [\[CrossRef\]](#)